RSC Advances

PAPER

View Article Online
View Journal | View Issue

Cite this: *RSC Adv.*, 2016, **6**, 23961

Reduction of persistent photoconductivity in a few-layer MoS_2 field-effect transistor by graphene oxide functionalization

Neha Rathi,†[a] Servin Rathi,†[a] Inyeal Lee,[a] Jianwei Wang,[b] Moonshik Kang,[ac] Dongsuk Lim,[d] Muhammad Atif Khan,[a] Yoontae Lee[a] and Gil-Ho Kim*[a]

Received 5th February 2016
Accepted 20th February 2016

DOI: 10.1039/c6ra03436e

www.rsc.org/advances

We functionalized two-dimensional few-layer MoS_2 based FET with graphene oxide (GO) in order to improve its persistent photoconductivity and photoresponse time. Both pristine and GO functionalized devices show n-type semiconductor behavior with high on/off ratio exceeding $\sim 10^5$. The photoresponse of the GO–MoS_2 hybrid device shows almost complete recovery from persistent photoconductivity and a substantial decrease in response time from ~15 s in the pristine MoS_2 device to ~1 s in the GO–MoS_2 device. The reasons behind this improvement have been explored and discussed on the basis of electrostatic and photo interaction between GO and MoS_2. As GO is a strong candidate for various sensing applications, therefore this intelligent hybrid system, where GO interacts electrostatically with the underlying MoS_2 channel, has tremendous potential to add more functionalities to a pristine MoS_2 device for realizing various smart nanoscale FET-based biochemical and gas sensors for myriad applications.

Introduction

Two-dimensional (2D) material based heterostructures consisting of various combinations like graphene–MoS_2 and MoS_2–WSe_2 have resulted in various new device architectures for novel applications and transport studies.[1–7] Of these heterostructures, those involving MoS_2 are of particular interest due to their multi-functional properties, such as decent mobility, good photoresponsivity, and application in bio, and gas sensing.[8–11] The photo applications of MoS_2 and its heterostructures have attracted particular attention due to their highly responsive photo-detecting properties, however, various issues such as persistent photoconductivity (PPC) have plagued the photoresponse of MoS_2 based photodetectors.[2,7,12–15] Recently, several studies have point out the role of defects and sulfur vacancy within the material which can trap the photo activated carriers resulting in a longer recombination lifetimes, thus leading to PPC, however the role of interface charge and defects at SiO_2 and air interface with MoS_2 can also play detrimental effect in prolonging PPC.[12,13,15] Although, several methods like measurement in vacuum and encapsulating MoS_2 layers have been demonstrated to reduce PPC but a practical and simple method is still evading.[15] Further, heterostructures constituting 2D materials involves complex device fabrication and process intensive techniques which make them impractical for scalable production thereby limiting the application scope for such devices. In the present study, we have proposed and demonstrated a facile fabrication method which involves direct deposition of graphene oxide (GO) onto MoS_2 layers to address the critical issue of PPC in MoS_2 based devices. The fabricated devices with GO show comparative electrical characteristics after GO deposition and negligible PPC as compared to pristine MoS_2 devices, which display considerable PPC in their photocurrent. In addition to improving the photo properties, such hybrid devices holds huge potential to add further functionalities which can be readily applied for other applications like gas, bio and chemical sensing.

Experimental

GO solution preparation

GO nanostructures used in the experiment were synthesized using a modified Hummer's method. In this method, 4 g of graphite flakes were added to a 250 mL round-bottom flask containing 120 mL of H_2SO_4 and stirred for 1 h. A $KMnO_4$ aqueous solution was added to the mixture every 20 min while stirring. The mixture was then slowly heated to, and maintained at 40 °C for 5 h in order to oxidize the graphite. Subsequently,

[a]*School of Electronic and Electrical Engineering, Sungkyunkwan Advanced Institute of Nanotechnology (SAINT), Sungkyunkwan University, Suwon 16419, South Korea. E-mail: ghkim@skku.edu*

[b]*School of Mechanical and Electrical Engineering, Guizhou Normal University, Guiyang, 550002, China*

[c]*Manufacturing Engineering Team, Memory Division, Samsung Electronics Co., Hwasung 18396, South Korea*

[d]*School of Advanced Materials Science and Engineering, Sungkyunkwan University, Suwon 16419, South Korea*

† N. R. and S. R. are equal contributing authors.

150 mL of deionized (DI) water was added to the mixture followed by 17 mL of H_2O_2 solution while stirring for 30 min. This mixture was maintained at 40 °C for 24 h and then centrifuged. The resultant mixture was enclosed in a dialysis tube and washed repeatedly with ultrapure DI water in order to obtain a pH level of 5. Finally, the GO was dried in a freeze dryer at −60 °C for 48 h. Before using the GO solution in the experiment, the solution was ultra-sonicated for 24 h to reduce the size of GO flakes and then filtered. Approximately 1 nm-thick, few microns-wide GO nanostructures were obtained after ultra-sonication.[16,17]

MoS_2 flakes

The MoS_2 flakes used in the experiment were produced by standard mechanical exfoliation using the Scotch method from commercial bulk MoS_2 purchased from 2D semiconductors.

Characterization

In order to confirm the quality (chemical bonding, electrical and structural properties) of MoS_2 and GO layers, XPS (X-ray photoelectron spectroscopy) (ESCA 2000, VG Microtech, UK) was carried using twin anode X-ray sources Kα (1486.6 eV)/Mg Kα (1253.6 eV) in a vacuum of 10^{-9} Torr, whereas Raman spectra was obtained at room temperature using a WITec Raman microscope with a 532 nm laser.

MoS_2 FET device fabrication

The devices for the study were fabricated using exfoliated MoS_2 transferred directly on a 290 nm SiO_2–Si wafer by Scotch tape transfer technique. Before MoS_2 transfer, the wafers were treated with 100 W O_2 plasma for 60 seconds so to clean the wafers from any polymer or organic residues. After MoS_2 transfer, photoresist was spin coated at 4500 rpm for 30 seconds followed by 90 °C annealing. At this stage a required mask was loaded onto UV based mask aligner system (MDA-40FA). This was followed by typical UV photo lithography double exposure for defining contact region and the required pattern was then developed in PR developer, thereby the developed pattern was put in for metal deposition, where Ti/Au (10/70 nm) was deposited by e-beam metal deposition system. Finally, the lift-off in acetone gives the required metal pattern with electrical contacts and pads for probe and measurement. Before measurement, the devices were annealed at 300 °C in argon ambient for 30 min to enhance the metal–MoS_2 interface contact quality for good ohmic contacts with lower resistance.[3]

GO–MoS_2 hybrid FET fabrication

For this, the pristine MoS_2 devices were processed with the basic UV photo lithography steps to patterned the metal contact region with a few micrometer overlapping in the channel region, this was done to avoid doping at the metal–MoS_2 contact regions which otherwise results in bad ohmic contacts behavior. The UV photo lithography results in opening up the channel region in the pristine MoS_2 device. In this region, a 0.2 μL of graphene oxide solution (0.5 mg mL^{-1}) was drop casted using a micro-pipette and allowed to dried in ambient conditions, followed by cleaning in iso-propyl alcohol (IPA) and drying using N_2 gun.

Measurements

The electrical characteristics were measured using Keithley 4200 SCS at room temperature in ambient conditions. For photocurrent, the device was globally illuminated with a laser wavelength of 450 nm and power of 0.1 mW.

Results and discussion

Optical characterization

In order to confirm the quality of MoS_2 and GO layers, XPS and Raman analysis was carried out.

Fig. 1a shows the XPS spectrum of the MoS_2 layers on SiO_2–Si substrate, where the Mo 3d shows two peaks at 232.2 eV and 229 eV, which are attributed to the doublet of Mo $3d_{3/2}$ and Mo $3d_{5/2}$. The peaks at 161.9 eV and 162.9 eV indicate the binding energy for S $2p_{3/2}$ and S $2p_{1/2}$, respectively. These binding energies for Mo and S are in good agreement with the reported values.[18] Fig. 1b shows the deconvoluted C 1s peaks after Gaussian–Lorentzian fitting and Shirley background corrections. As seen from the figure, various functional groups associated with GO can be inferred from its XPS spectra, where oxygen based carboxyl, hydroxyl and epoxy groups in GO can be identified by their peak position in the deconvoluted XPS spectra, C–C peak at 284.6 eV, C–O peak at 286.6 eV, C═O peak at 288 eV and COOH peak at 289 eV. These values are in good agreement with the published results.[16,17] Further, Fig. 1c shows the Raman spectra for both MoS_2 and GO where the difference between the E^1_{2g} (385.3 cm^{-1}) and A_{1g} (410.1 cm^{-1}) peaks show that the exfoliated layer is composed of a few layer MoS_2 (5–6 layers), whereas the Raman peaks of GO can be identified as D and G peaks at 1340 cm^{-1} and 1563 cm^{-1} which are related to defects and relative degree of graphitization in GO. In addition to D and G peaks, broad bands/peaks appear in the high frequency end of the spectrum, in the range of 2690–2300 cm^{-1}, which are usually composed of D peak overtones and combination of D and G peaks, named as 2D, D + G and 2D′. The observed peaks and band in the GO Raman spectra are also in agreement with the other published results.[17,19] Fig. 1d shows the Raman spectra of MoS_2 layer before and after the GO deposition. It can be seen clearly that the spectra is shifted to the right and this blue shift in the A_{1g} peak of MoS_2 spectra has been associated with p-type doping whereas a similar shift in E^1_{2g} peak is the indicator of compressive strain in the layer.[18,20] It may be noted that not all the samples show such a large shift in E^1_{2g}, since, GO soln contracts while drying, therefore this peak shift can depend on various factors like number of GO layers, van der Waals interaction between GO and MoS_2 *etc.* Additionally, in some samples Raman measurement on GO–MoS_2 was followed by black spot formation, which may be associated with the reduction of GO layers due to thermal heating from the laser power, however such devices were discarded for electrical and photocurrent measurements.

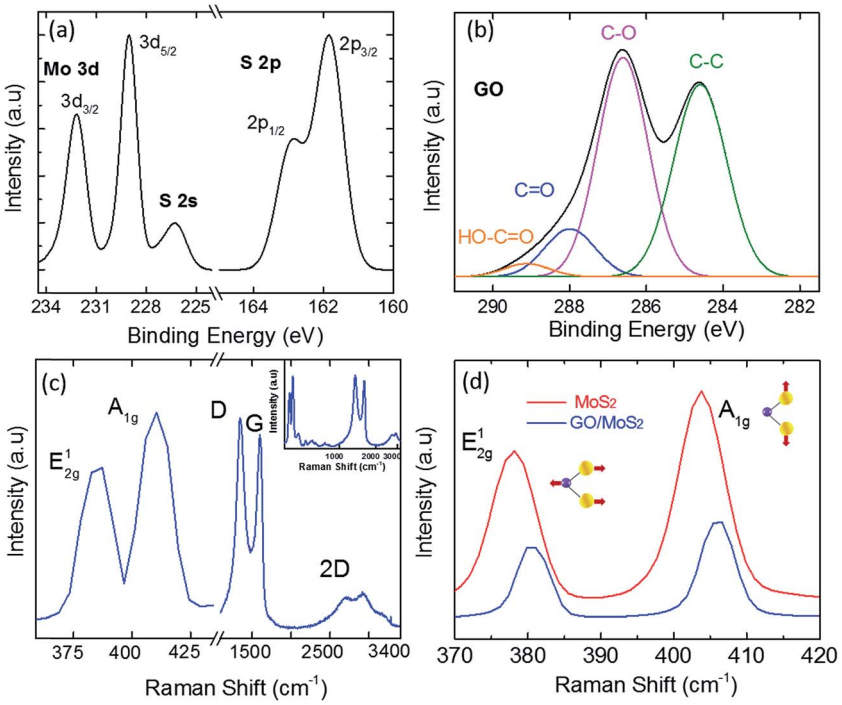

Fig. 1 Optical characterization of GO and MoS_2 material. (a and b) XPS peaks of a MoS_2 flake showing 3d and 2p peaks and carbon peaks of GO flakes, respectively (c) Raman spectra of MoS_2 and GO with the inset showing wide scan profile (d) Raman spectra of a pristine MoS_2 and after GO deposition.

Electrical measurement

Fig. 2a, c and d, show schematic and microscopic image of the fabricated MoS_2 based device on SiO_2–Si substrate. After measurements with the pristine device, the device was processed to pattern metal contacts region with photoresist, followed by GO deposition, resulting in the hybrid GO–MoS_2 device. Fig. 2b and e show the schematic and microscopic image of such a device where a visible color contrast indicates the

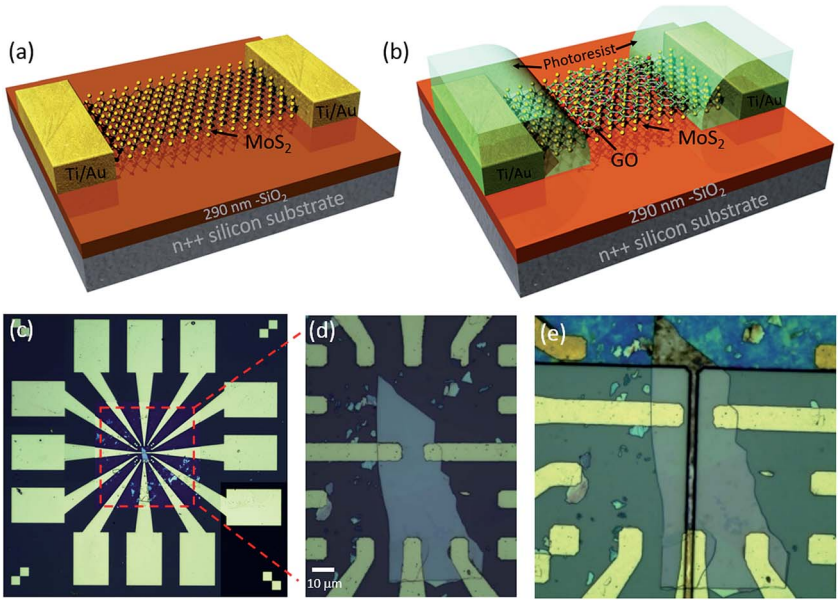

Fig. 2 Schematic and device microscopic image of the fabricated device. Schematic of (a) pristine MoS_2 device and (b) GO covered channel with photoresist covering the vicinity of the contact area of the hybrid device, (c and d) fabricated device chip where the zoom in microscopic image showing the exfoliated few-layer MoS_2 connected by the Ti/Au metal contacts. (e) GO–MoS_2 hybrid device where the contacts edge parts were first patterned with photoresist followed by GO deposition.

dried GO solution in the photoresist defined region. The electrical characteristics, measured by Keithley 4200 SCS at room temperature in ambient conditions, are shown in Fig. 3, where Fig. 3a plots drain current (I_{ds}) *versus* drain voltage (V_{ds}) at various gate voltages (V_{gs}), ranging from −40 to 40 V. The linear curves obtained indicate the formation of ohmic-like contacts due to low barrier height at the metal–MoS_2 interface.[21] The transfer characteristics are plotted in Fig. 3b at different drain voltages. As seen from Fig. 3b, the device operates in depletion mode, where a free carrier density exists at zero gate voltage and can be modulated further by sweeping the gate voltage. The existence of free electrons density in MoS_2 has been attributed to various factors like sulphur vacancy or substitutional doping by impurities.[22] In addition to other device parameters like threshold voltage and subthreshold slope (SS), the field-effect mobility (μ_{fe}) can be obtained from the transfer characteristics using the following expression:

$$\mu_{fe} = \frac{L}{WC_{ox}V_{ds}}\frac{dI_{ds}}{dV_{bg}}, \quad (1)$$

where, L and W are the device channel length and width, respectively, V_{ds} is the applied drain bias, $\frac{dI_{ds}}{dV_{bg}}$ is the transconductance and C_{ox}, capacitance per unit area, is given by $\frac{\varepsilon_0\varepsilon_r}{d}$ (ε_0 is the absolute permittivity and ε_r is the dielectric constant of SiO_2 of thickness d) and for 290 nm-thick SiO_2 is 1.19×10^{-8} F cm^{-2}. The field-effect mobility calculated at room temperature vary in the range of 30–40 $cm^2\ V^{-1}\ s^{-1}$ for a batch of 10 devices. Among other device metrics, the sub-threshold slope, as measured from the inverse slope of semi-log transfer plot, and I_{on}/I_{off} ratio varies in the range of 1.5 to 2 V dec^{-1}, and 10^5 to 10^6, respectively. The obtained values are in agreement with the published literature and demonstrate high quality of the fabricated devices.[23,24]

Fig. 3c and d show the electrical measurement results for GO–MoS_2 hybrid devices. As seen from XPS and Raman analysis that in GO, the sp^2 hybridized carbon grid is partially oxidized to carboxyl, hydroxyl and epoxy groups, which are known for their protonic doping capabilities[25] and therefore can deplete carriers in the underneath MoS_2 channel. The energy band diagrams illustrating the depletion and lateral channel transport are shown in Fig. 4. GO behave as a wide band gap insulator, with band gap varying from 2.7 eV to 0.7 eV, with localized

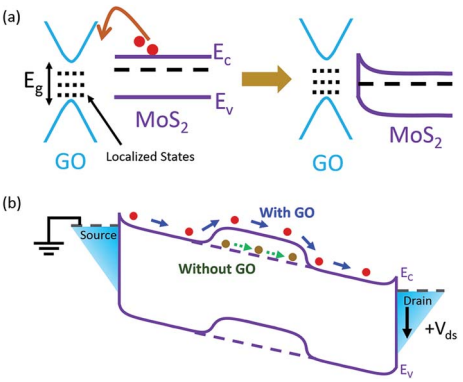

Fig. 4 (a) Schematic energy band diagram at the GO–MoS_2 junction before and after GO deposition (b) band diagram showing lateral electron transport before and after GO deposition in the GO–MoS_2 hybrid device.

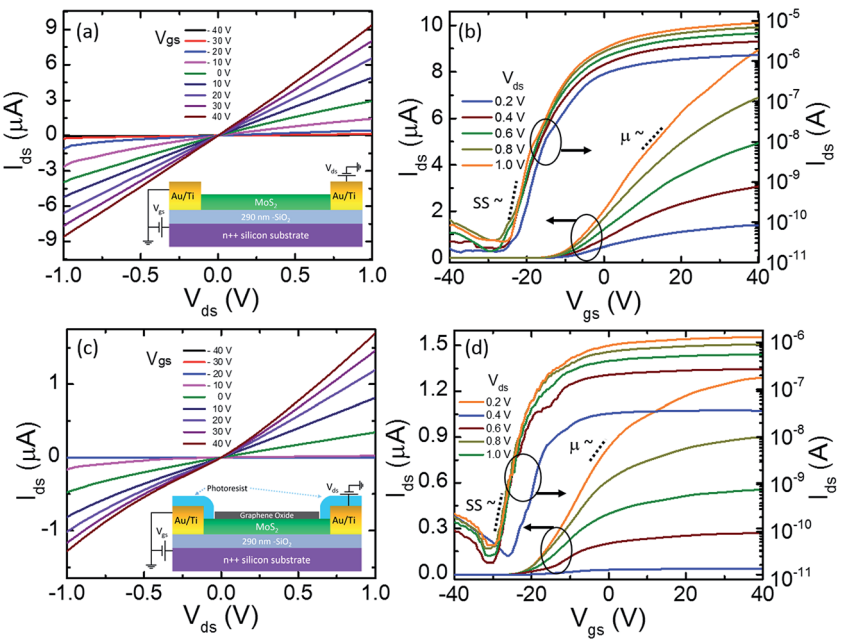

Fig. 3 (a) I_{ds}–V_{ds} at various V_{gs} and (b) transfer (I_{ds}–V_{gs}) characteristics of a few-layer pristine MoS_2 transistor at various V_{ds} (c) I_{ds}–V_{ds} at various V_{gs} and (d) transfer (I_{ds}–V_{gs}) characteristics of the GO–MoS_2 hybrid device. The inset in (a) and (c) show schematic image of the device and dashed lines in (b) and (d) mark the sub-threshold slope and mobility measurement point as obtained from the slope of semi-log and natural curve, respectively.

energy states whose energy and density depend on various factors like concentration of sp^2–sp^3 domains and clusters.[25–27] Due to this unique property of GO, free carriers from MoS_2 are transferred to GO leading to a barrier formation all along the lateral overlap plane of the channel region. This band bending not only results in the decrease in carrier concentration, thus high resistance to current flow in the form of higher energy barrier under the GO overlap region, but also reduces the carrier mobility due to remote ionized or Coulomb scattering from the GO layer. These expected characteristics of Go–MoS_2 device are also evident from Fig. 3c and d, where current in the device drops by almost an order after depositing GO layers on the top of MoS_2 layer. Although, it led to a decrease in the mobility from 30 to 10 $cm^2\ V^{-1}\ s^{-1}$ but other device metrics like SS and I_{on}/I_{off} ratio did not varies much. The role of photoresist covering the vicinity of metal contacts can be understood from Fig. 4a where if the contact region were also allowed to be covered by GO, would have resulted in critical drop in the device performance metrics like channel current, ohmic-like behavior, *etc.* due to high Schottky barrier formation at the metal contacts thus leading to very high contact resistance.[28,29]

Photocurrent measurement

Fig. 5a–d show photocurrent measurement at various drain voltage with global illumination by 450 nm laser wavelength for both pristine and hybrid devices. The incident of photons leads to generation of electron and hole pairs which turn on the device in the off-region as well. The observed photo gating effect *i.e.*, the shifting of threshold voltage to a higher gate voltage, has been attributed to shallow traps near the valence band edge, which on excitation becomes positively charged, thus photo gating the device.[15,30,31] The photocurrent, obtained by subtracting the corresponding dark current from the illuminated current, is plotted in Fig. 5b, where it can be seen that the photocurrent varies with gate voltage, initially rising very fast and start saturating after reaching a certain peak value.

Various explanation have been proposed for this photo behavior including quasi-fermi level position dependent recombination rate, gate induced carrier concentration and its mobility dependency *etc.*[15,30] Similarly, Fig. 5c and d show photo behavior of GO–MoS_2 device with gate voltage. It can be seen that despite an initial current drop in GO–MoS_2 device, the gate bias dependent photocurrent display a pattern similar to that of

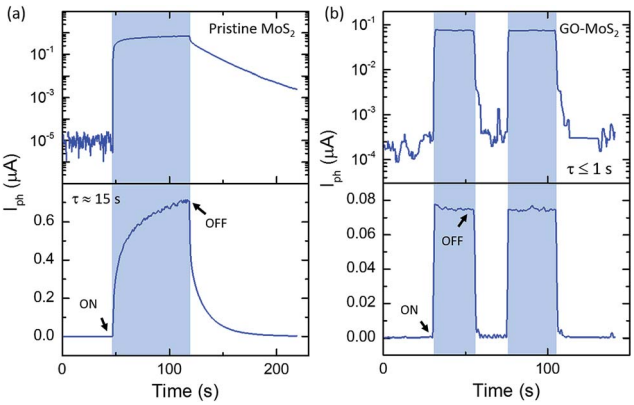

Fig. 6 (a and b) Photocurrent response plotted in dual panel linear and semi-log scale for pristine and GO–MoS_2 devices, respectively.

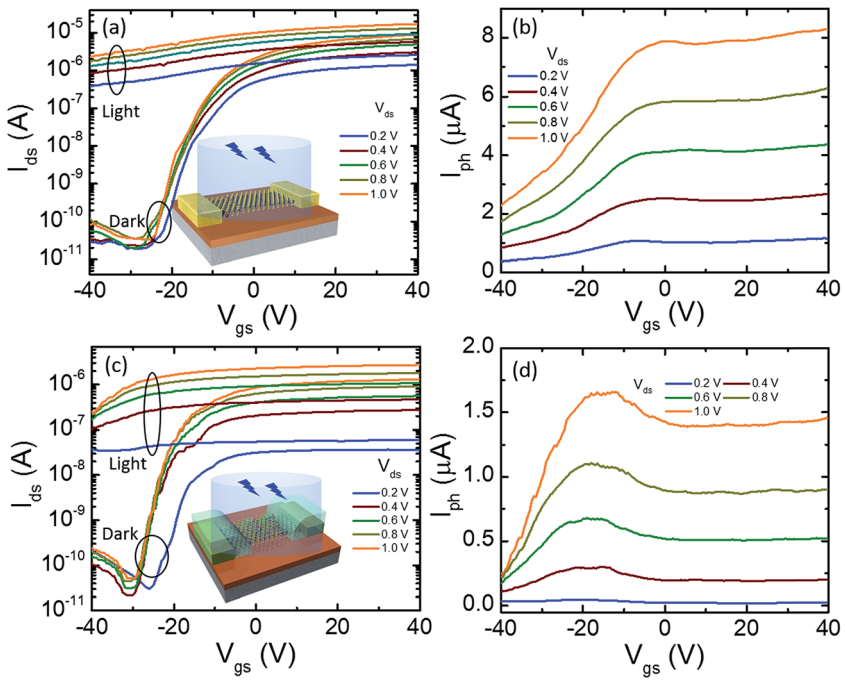

Fig. 5 (a) Transfer characteristics (I_{ds}–V_{gs}) with dark and illuminated current with (b) showing the photocurrent variation with gate voltage at various V_{ds} for the pristine MoS_2 (c) transfer characteristics (I_{ds}–V_{gs}) with dark and illuminated current with (d) showing the photocurrent variation with gate voltage at various V_{ds} for GO–MoS_2 hybrid device.

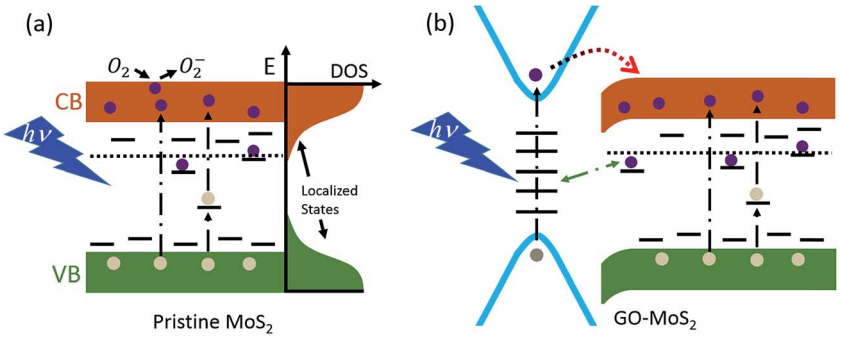

Fig. 7 (a) Schematic energy band diagram of MoS_2 showing generation and recombination process under laser illumination. In the ambient conditions, the interface can adsorb ambient species like gases and moisture which also play role in observed PPC in devices (b) band diagram showing photo generation and recombination in the GO–MoS_2 device illustrating the role of GO in photoresponse and reduced PPC.

pristine MoS_2 device, however with exceptions of showing peak photocurrent at an early gate voltage and comparatively higher photocurrent saturation.

To further investigate the photo behavior of these devices, time-dependent photoresponse was also measured. As can be seen from Fig. 6a, the pristine MoS_2 device shows huge PPC as the current in the channel do not recover back to its original value even after a prolong time period. In comparison, the photoresponse of GO–MoS_2 device, in Fig. 6b, shows a completely different behavior, with the photoresponse time decreasing sharply from an approx. 15 s to less than equal to 1 s and the device shows negligible PPC. Several factors like charge trapping at the interface, adsorbed impurities like gases or moisture from ambient environment, material defects and impurities have been attributed for the occurrence of PPC in MoS_2,[12,14] as shown in the schematic of Fig. 7a. Although, various methods like passivation by high-k dielectric or measurement in vacuum conditions have shown to reduce the PPC,[13,15] but the technique of GO deposition in MoS_2 devices leverage the wide band gap of GO interspersed with localized states to minimize the PPC in MoS_2 based devices. One of the possible explanation of the reasons behind this improvement, as illustrated in Fig. 7b, is a complex process of photo-activity in GO layers, which acts in a completely different way than simply trapping electrons from the MoS_2 layers. Upon illumination and depending on the energy levels, the photo-generated carriers in GO can be transferred to MoS_2 or can recombine within GO through various recombination process like SRH (Shockley–Read–Hall), Auger and trap/localized states assisted recombination,[25] whereas the photo-generated carriers in MoS_2 can also have additional recombination mechanism *via* GO localized states apart from the typical recombinations. Due to these active and additional recombination/generation mechanism at the GO–MoS_2 interface, the trapping of electrons on the ambient MoS_2 by atmospheric gases like O_2 and H_2O is suppressed which results in the reduction of PPC. Similarly, when the illumination is off, the active recombination centers in GO can results in quick photoresponse of approx. 1 s, thus resulting in negligible PPC in the GO–MoS_2 device.

Conclusions

In summary, GO–MoS_2 hybrid devices were fabricated and studied for variation in photo responses. The GO–MoS_2 device maintains reasonable I_{on}/I_{off} ratio and subthreshold slope as compared to pristine MoS_2 device. The photocurrent response demonstrates a substantial decrease in response time and almost complete recovery from PPC effect. The device properties and photoresponse can be improved further by optimizing the GO concentration ratio and deposition thickness. Further, the observed electrostatical interaction of GO layer with the underlying MoS_2 channel can be utilized to load additional functionalities to a pristine device, especially for sensing non-polar gases like H_2 and other chemical and biological entities.

Acknowledgements

This research was supported by Basic Science Research Program through the National Research Foundation of Korea (NRF) funded by the Ministry of Education, Science and Technology (2013R1A2A2A01069023 and 2014R1A1A1004632).

References

1 J. Wu, W. Walukiewicz, K. M. Yu, J. W. Ager, E. E. Haller, H. Lu, W. J. Schaff, Y. Saito and Y. Nanishi, *Appl. Phys. Lett.*, 2002, **80**, 3967.
2 W. J. Yu, Y. Liu, H. Zhou, A. Yin, Z. Li, Y. Huang and X. Duan, *Nat. Nanotechnol.*, 2013, **8**, 952–958.
3 S. Rathi, I. Lee, D. Lim, J. Wang, Y. Ochiai, N. Aoki, K. Watanabe, T. Taniguchi, G.-H. Lee, Y.-J. Yu, P. Kim and G.-H. Kim, *Nano Lett.*, 2015, 150619104057003.
4 K. Roy, M. Padmanabhan, S. Goswami, T. P. Sai, G. Ramalingam, S. Raghavan and A. Ghosh, *Nat. Nanotechnol.*, 2013, **8**, 826–830.
5 O. Lopez-Sanchez, D. Lembke, M. Kayci, A. Radenovic and A. Kis, *Nat. Nanotechnol.*, 2013, **8**, 497–501.
6 H. Yang, J. Heo, S. Park, H. J. Song, D. H. Seo, K.-E. Byun, P. Kim, I. Yoo, H.-J. Chung and K. Kim, *Science*, 2012, **336**, 1140–1143, DOI: 10.1126/science.1220527.

7 C. Shih, Q. H. Wang, Y. Son, Z. Jin, D. Blankschtein and M. S. Strano, *ACS Nano*, 2014, 1–8.
8 D.-W. Lee, J. Lee, I. Y. Sohn, B.-Y. Kim, Y. M. Son, H. Bark, J. Jung, M. Choi, T. H. Kim, C. Lee and N.-E. Lee, *Nano Res.*, 2015, 2–5.
9 Q. Y. Ren, W. D. Hutchison, J. L. Wang, S. Muñoz Pérez, J. M. Cadogan and S. J. Campbell, *Phys. Status Solidi A*, 2014, **211**, 2898–2899.
10 X. Cui, G.-H. Lee, Y. D. Kim, G. Arefe, P. Y. Huang, C.-H. Lee, D. a. Chenet, X. Zhang, L. Wang, F. Ye, F. Pizzocchero, B. S. Jessen, K. Watanabe, T. Taniguchi, D. a. Muller, T. Low, P. Kim and J. Hone, *Nat. Nanotechnol.*, 2015, 1–7.
11 W. Zhang, J.-K. Huang, C.-H. Chen, Y.-H. Chang, Y.-J. Cheng and L.-J. Li, *Adv. Mater.*, 2013, **25**, 3456–3461.
12 K. Cho, T.-Y. Kim, W. Park, J. Park, D. Kim, J. Jang, H. Jeong, S. Hong and T. Lee, *Nanotechnology*, 2014, **25**, 155201.
13 Y.-C. Wu, C.-H. Liu, S.-Y. Chen, F.-Y. Shih, P.-H. Ho, C.-W. Chen, C.-T. Liang and W.-H. Wang, *Sci. Rep.*, 2015, **5**, 11472.
14 K. Roy, M. Padmanabhan, S. Goswami, T. P. Sai, G. Ramalingam, S. Raghavan and A. Ghosh, *Nat. Nanotechnol.*, 2013, 1–5.
15 D. Kufer and G. Konstantatos, *Nano Lett.*, 2015, **15**, 7307–7313, DOI: 10.1021/acs.nanolett.5b02559.
16 J. Wang, S. Rathi, B. Singh, I. Lee, H.-I. Joh and G.-H. Kim, *ACS Appl. Mater. Interfaces*, 2015, 150617152223006.
17 J. Wang, S. Rathi, B. Singh, I. Lee, S. Maeng, H.-I. Joh and G.-H. Kim, *Sens. Actuators, B*, 2015, **220**, 755–761.
18 C. Chen, H. Qiao, S. Lin, C. Man Luk, Y. Liu, Z. Xu, J. Song, Y. Xue, D. Li, J. Yuan, W. Yu, C. Pan, S. Ping Lau and Q. Bao, *Sci. Rep.*, 2015, **5**, 11830.
19 P. Cui, J. Lee, E. Hwang and H. Lee, *Chem. Commun.*, 2011, **47**, 12370.
20 Y. Shi, J.-K. Huang, L. Jin, Y.-T. Hsu, S. F. Yu, L.-J. Li and H. Y. Yang, *Sci. Rep.*, 2013, **3**, 1839.
21 J. Na, M. Shin, M. K. Joo, J. Huh, Y. Jeong Kim, H. Jong Choi, J. Hyung Shim and G. T. Kim, *Appl. Phys. Lett.*, 2014, **104**, 26–31.
22 S. Qin, W. Lei, D. Liu and Y. Chen, *Sci. Rep.*, 2014, **4**, 7582.
23 H. Y. Chang, W. Zhu and D. Akinwande, *Appl. Phys. Lett.*, 2014, **104**, DOI: 10.1063/1.4868536.
24 D. Jariwala, V. K. Sangwan, D. J. Late, J. E. Johns, V. P. Dravid, T. J. Marks, L. J. Lauhon and M. C. Hersam, *Appl. Phys. Lett.*, 2013, **102**, 173107.
25 J. Shang, L. Ma, J. Li, W. Ai, T. Yu and G. G. Gurzadyan, *Sci. Rep.*, 2012, **2**, 792.
26 X. Wang, H. Tian, M. A. Mohammad, C. Li, C. Wu, Y. Yang and T.-L. Ren, *Nat. Commun.*, 2015, **6**, 7767.
27 M. a. Velasco-Soto, S. a. Pérez-García, J. Alvarez-Quintana, Y. Cao, L. Nyborg and L. Licea-Jiménez, *Carbon*, 2015, **93**, 967–973.
28 D. Kiriya, M. Tosun, P. Zhao, J. S. Kang and A. Javey, *J. Am. Chem. Soc.*, 2014, **136**, 7853–7856.
29 S. McDonnell, R. Addou, C. Buie, R. M. Wallace and C. L. Hinkle, *ACS Nano*, 2014, **8**, 2880–2888.
30 M. Buscema, J. O. Island, D. J. Groenendijk, S. I. Blanter, G. a. Steele, H. S. J. van der Zant and A. Castellanos-Gomez, *Chem. Soc. Rev.*, 2015, **44**, 3691–3718.
31 F. H. L. Koppens, T. Mueller, P. Avouris, a. C. Ferrari, M. S. Vitiello and M. Polini, *Nat. Nanotechnol.*, 2014, **9**, 780–793.